Check for updates

*Advanced Engineering Materials*

ADVANCED ENGINEERING MATERIALS
www.aem-journal.com

RESEARCH ARTICLE OPEN ACCESS

# Precipitation Simulations of the O-Phase in $Ti_2AlNb$ Alloys Processed by Laser Powder Bed Fusion

Silvana Tumminello[1] | Joachim Gussone[1] | Suzana G. Fries[1,2] | Marcus Rackel[3] | Andreas Stark[3] | Norbert Schell[3] | Jan Haubrich[1] | Guillermo Requena[1]

[1]Institute for Frontier Materials on Earth and in Space, German Aerospace Center (DLR), Cologne, Germany | [2]Materials Research Department, RUB, Bochum, Germany | [3]Helmholtz-Zentrum Hereon, Geesthacht, Germany

**Correspondence:** Silvana Tumminello (silvana.tumminello@dlr.de)

**Received:** 18 February 2026 | **Revised:** 11 May 2026 | **Accepted:** 14 May 2026

**Keywords:** interfacial energy | phase transformations | precipitation | sensitivity analysis

## ABSTRACT

In this work, computational models for phase precipitation were used to simulate the evolution of the O-phase volume fraction during postprocessing of a Ti-21Al-25Nb (at.%) alloy processed by laser powder bed fusion and to study the phase transformations during subsequent heat treatments. The combination of computational simulations, thermodynamic models, and own experimental analysis allowed us to understand the sluggishness of the O-phase isothermal precipitation in this alloy. To arrive at these conclusions and ensure that the simulations provided meaningful results, a thorough analysis of the input parameters was required to set up the calculations. A sensitivity analysis allowed quantification of the influence of these parameters on the phase fraction evolution. The interfacial energy of the matrix and precipitate phases was identified as the most relevant input parameter for the simulation of the volume fraction evolution during the aging process. This case study illustrates that computational thermodynamic and precipitation analysis provides a strong complementarity with experimental studies, enabling to tackle specific questions that are difficult to answer by designed experiments and even predict materials' behavior.

## 1 | Introduction

Simulations of solid-state precipitation kinetics contribute to the understanding of microstructure formation and, thus, play an important role in the design of thermal processing routes to tailor multiphase microstructures. Progress in engineering applications of materials still requires a better understanding of composition–microstructure–property relationships to accelerate materials development and their processing. This is the core of the Integrated Computational Materials Engineering (ICME) framework that systematically links experiments and computational models to materials design [1–3].

Simulations of precipitation kinetics are based on nucleation, growth, and coarsening models, which in turn require properly coupled thermodynamic and mobility descriptions as implemented in a number of simulation packages, including the Thermo-Calc (TC) software [4, 5]. However, the sensitivity of the results to the input settings in these calculations is very high, and thus the models and parameters require a critical analysis in order to

**Abbreviations:** A1, face-centered cubic structure fully disordered, γ. Thermo-Calc phase name FCCA1.; $L1_2$, face-centered cubic structure ordered, γ′. Thermo-Calc phase name FCC_L12.; $L1_0$, face-centered cubic structure ordered, γ in Ti alloys. Thermo-Calc phase name FCC_L10.; A2, body-centered cubic structure fully disordered, β. Thermo-Calc phase name BCC_A2.; B2, body-centered cubic structure fully ordered, βo. Thermo-Calc phase name BCC_B2.; **BSE**, Backscatter Electron; **CALPHAD**, CALculation of PHAse Diagrams; **EDS**, Energy Dispersive Spectroscopy; **HEXRD**, High-Energy synchrotron X-ray Diffraction; **ICME**, Integrated Computational Materials Engineering; **IE**, Interfacial Energy; **LAGB**, Low-Angle Grain Boundaries; **LPBF**, Laser Powder Bed Fusion; **LSW**, Lifshitz–Slyozov–Wagner; **MSE**, Mean Square Error; **ND**, Nucleation site Density; **PSD**, Particle Size Distribution; **SEM**, Scanning Electron Microscopy; **SL**, Sub-Lattice; **TC**, Thermo-Calc; **TC-Prisma**, Thermo-Calc Precipitation Module; **TDB**, Thermodynamic Database; **TEM**, Transmission Electron Microscopy.

This is an open access article under the terms of the Creative Commons Attribution License, which permits use, distribution and reproduction in any medium, provided the original work is properly cited.

© 2026 The Author(s). *Advanced Engineering Materials* published by Wiley-VCH GmbH.

obtain meaningful results [6]. The input parameters must be derived for all present phases, i.e., matrix and precipitating phases, under different conditions. Among others, necessary input parameters for precipitation are nucleation site density (ND), elastic properties, dislocation density, elastic interfacial energy (IE), shape of precipitate, and transformation strain. Although they can be crucial to simulate real precipitation processes, they are often not well known, even for simple systems; therefore, they require educated choices. Experimental studies not only provide the necessary data to derive the parameters, but also validate the approximations made and enable moving from reproduction of experimental observations to providing a deeper understanding or even prediction of behavior under conditions not yet characterized.

In many cases, coprecipitation needs to be considered, but multiple precipitating phases increase the complexity and number of input parameters.

With the introduction of additive manufacturing, more recently an interest developed in processing $Ti_2AlNb$ alloys by laser powder bed fusion (LPBF) [7–10]. LPBF opens new possibilities for processing these lightweight structural alloys, but the as-built material obtained after manufacturing usually requires a suitable postprocessing treatment. Several different LPBF and postprocessing conditions producing different microstructures have been explored in our previous work [11].

In the present work, the evolution of the O-phase volume fraction during postprocessing, aging at 600°C for 3 h, of an LPBF Ti-21Al-25Nb (at.%) alloy was investigated by in situ high-energy synchrotron X-ray diffraction (HEXRD). Under these conditions, the obtained microstructure was determined to contain only the β phase as matrix with O-phase precipitates, hence presenting a suitable scenario for a thermodynamic-based precipitation simulation study, as no coprecipitation occurs.

The objective of this work is twofold: i) to reproduce the phase fraction evolution of the O-phase observed experimentally by means of kinetic simulations to identify the most relevant parameters driving the precipitation of this phase. ii) To analyze the influence of each input parameter on the precipitation evolution simulated by thermodynamic and kinetic models by carrying out a sensitivity analysis. Both objectives contribute to gaining confidence in the simulation setup before being able to predict the materials' behavior under new conditions.

A short literature review on the $\beta_o$ to O-phase transformation is presented here to understand its main features, type of transformation, crystallography, and microstructure. Moreover, we highlight how this knowledge has been captured in the CALculation of PHAse Diagrams (CALPHAD) thermodynamic models encoded in the thermodynamic database (TDB) used in this work. This knowledge also guided the decisions on the input parameters for precipitation simulations on the Ti-21Al-25Nb (at.%) alloy.

### 1.1 | Literature Review on $\beta_o$ (B2) → O Phase Transformation

The O-phase crystal lattice has a Pearson symbol *oC16*, space group *Cmcm*, NaHg prototype, and composition based on the stoichiometry $Ti_2AlNb$ [12, 13]. Alloys containing a significant volume fraction of the O-phase embedded in a β (A2) matrix are strengthened mainly by this orthorhombic phase responsible for the favorable mechanical properties, i.e., high creep resistance, balanced strength and ductility at high and room temperature, due to the multiple slip systems that can be activated in the orthorhombic crystal lattice [14–16].

The $\beta/\beta_o \rightarrow$ O phase transformation pathways have been intensively studied by Bendersky et al. [17–20]. Based on experimental examination of the $\beta/\beta_o$ and $\beta_o$/O interfaces with transmission electron microscopy (TEM) and crystallographic knowledge, the authors proposed in line with the Landau theory of phase transformations [21], that phase transformations in the $Ti_2AlNb$ alloys occur following paths of related crystal structures (in *Strukturbericht* notation: **A2** - BCC disordered, β-, **B2** - BCC ordered, $\beta_o$-, **B19** - orthorhombic -, **A20** - face centered orthorhombic -, **A3** - HCP disordered -, **D0$_{19}$**- HCP ordered -, **O**) as a reduction of the symmetry from highly symmetric and fully disordered A2 down to the low symmetry orthorhombic phase O passing through metastable intermediate states like B19, or stable ones like $D0_{19}$ or A3 depending on the parent phase composition and ultimately on the processing route.

The approach of Bendersky et al. assumes coherent and no long-range diffusion transformations, which likely hold for the Ti–Al–Nb system in the composition considered here. The $\beta/\beta_o \rightarrow O$ transformation in the Ti–Al–Nb system has been observed to occur with a wide range of characteristics such as, short-range diffusion, some degree of ordering of the parent phase $\beta_o$ (B2) or displacive (without composition changes), depending on the alloy composition, which results in different transformation paths of either first or second order behavior [22].

In terms of kinetics, the $\beta_o \rightarrow O$ transformation was observed to be relatively sluggish [18, 20], apparently with extensive nucleation of O-phase followed by growth until precipitate impingement (wavy interfaces) hindering the continuation of uniform growth [18]. However, when the transformation follows certain paths, it can also have fast precipitation kinetics favored by high cooling rates during alloy processing that leads to supersaturation of the parent phase [22].

Furthermore, the same authors analyzed the domain orientations at interfaces as a critical aspect that determines the transformation path. The orientation relation between the crystal lattices of $\beta_o$ and O-phase is known to be $[011]_{B2}//[001]_O$ and $[1\bar{1}1]_{B2}//[110]_O$ with a unit cell volumes ratio 8:1 [12, 18, 23]. Additionally, some degree of interfacial coherency is present due to the crystallographic orientation relation that results in the formation of transformation stresses at the $\beta_o$/O interface. As a consequence of the types of interfaces, the morphology of the O-phase precipitates in the final microstructure varies with processing conditions and alloy composition. In particular, O-phase precipitates that grow into the $\beta_o$ (B2) phase matrix typically exhibit needle- or plate-like morphology. They often show crystallographic correlation with the formation and growth of neighboring precipitates, and are strongly influenced by cooling rate. Notably, plate-like precipitates tend to form stress–accommodating interfaces, whereas needle-like



15272648, 2026, 17, Downloaded from https://advanced.onlinelibrary.wiley.com/doi/10.1002/adem.70963 by Dtsch Zentrum F. Luft-U. Raum Fahrt In D. Helmholtz Gemein., Wiley Online Library on [06/10/2026]. See the Terms and Conditions (https://onlinelibrary.wiley.com/terms-and-conditions) on Wiley Online Library for rules of use; OA articles are governed by the applicable Creative Commons License

precipitates result in nonstress–accommodating interfaces, owing to the crystallographic rotational variants of the orthorhombic structure [18].

## 2 | Methods

### 2.1 | Experimental

#### 2.1.1 | Material Fabrication

The alloy investigated in this study was additively manufactured with LPBF using Ti-22Al-25Nb (at.%) powder produced by Helmholtz-Zentrum Hereon, Geesthacht, Germany. We chose specimens processed with an energy density of 89 J/mm3 and a preheating temperature of 150°C of the base plate because of the advantages of a low temperature LPBF combined with aging postprocessing. Further details on the LPBF processing can be found in [11].

The composition of the LPBF alloy, determined by energy dispersive spectroscopy (EDS), was close to Ti-21Al-25Nb (at.%) [11]. The main microstructure characteristics of the as-built specimens are summarized in Table 1.

#### 2.1.2 | High-Energy X-Ray Diffraction

In situ HEXRD was used to determine the phase fractions and lattice parameters as a function of aging time. HEXRD was performed in transmission mode with a beam energy of ≈100 keV ($\lambda$ = 0.124 Å) and a slit size of 0.8 × 0.8 mm$^2$ at the beamline P07-HEMS operated by Helmholtz-Zentrum Hereon at the synchrotron source PETRA III (Deutsches Elektronen-Synchrotron, DESY, Hamburg, Germany). A Perking Elmer XRD1621 (2048 × 2048 pixels) detector was used to obtain entire Debye–Scherrer rings with an exposure time of 0.1s, whereas 20 exposures were integrated and 10 images per minute were acquired.

The in situ heat treatment at 600°C during HEXRD was carried out for 3 h under vacuum (<$10^{-4}$ mbar) using a modified dilatometer Bähr DIL 805 A/D equipped with an induction furnace. The heating rate before the aging heat treatment was 100 K/min. For the evaluation of the diffraction data, the software FIT2D was used for calibration with a LaB6 standard and ring integration. Rietveld analyses were carried out for the determination of the phase fractions and lattice parameters with the software TOPAS from Bruker. The lattice parameters of β and O-phase were used to convert the phase fractions from weight to volume. The microstructure was investigated by scanning electron microscopy (SEM) with backscatter electron (BSE) detection mode in a FEI Helios Nanolab 600i dual beam (electron and Ga+) microscope.

### 2.2 | Computational

#### 2.2.1 | Precipitation Simulations

Simulations of precipitation kinetics of the O-phase were done using the TC Precipitation Module (TC-Prisma) [5] module

**TABLE 1** | Experimental characterization data of the Ti-21Al-25Nb (at.%) alloy before and after aging derived from our previous study [11].

| Experimental parameter | Value |
|---|---|
| Measured composition (EDS) | 53.5 Ti, 20.9 Al, 25.5 Nb (at.%) |
| ***As-built microstructure*** | |
| phase(s) | single phase $\beta/\beta_o$-(Ti,Al,Nb) |
| matrix Al initial supersaturation calculated as $\bar{x_{Al}}/x_{eq,Al}-1$ | $0.209/0.089-1=1.33$ |
| grain size | 100–200 µm |
| grain aspect ratio | 2 |
| melt pool crystallography | grains grow through |
| segregation | yes. Nb-depleted. |
| residual macrostresses | yes |
| deviatoric strain | 0.0027 |
| texture | <100>in the built direction |
| hardness | 335 ±16 HV0.2 |
| ***After aging 3 h 600°C*** | |
| phase(s) | O-phase + $\beta$-(Ti,Al,Nb) |
| volume fraction | 66% O-phase, 34% $\beta/\beta_o$ |
| precipitate shape | lenticular |
| precipitate size | 200–300 nm |
| precipitate aspect ratio average | 3–5 |
| segregation | yes. Nb-depleted. |
| hardness | 541 ± 23 HV0.2 |



15272648, 2026, 17, Downloaded from https://advanced.onlinelibrary.wiley.com/doi/10.1002/adem.70963 by Dtsch Zentrum F. Luft-U. Raum Fahrt In D. Helmholtz Gemein., Wiley Online Library on [06/10/2026]. See the Terms and Conditions (https://onlinelibrary.wiley.com/terms-and-conditions) on Wiley Online Library for rules of use; OA articles are governed by the applicable Creative Commons License

within the TC Software package version 2025a [4]. The thermodynamic and mobility databases for Ti-alloys TCTI6 and MOBTI5 were used [24, 25]. TC is a software that uses Gibbs energies descriptions for the phases of a material system properly encoded in TDBs constructed using the CALPHAD method [26]. The TC-Prisma simulates diffusion-controlled precipitation processes in multicomponent and multiphase systems. The models for nucleation and growth are based on the Langer–Schwartz theory [27] and the Kampmann–Wagner numerical method [28]. The nucleation model uses the maximum driving force method that fixes the composition of the nucleus for a given supersaturation of the matrix. The general growth rate model for interface velocity that assumes the quasi-steady state approximation and accounts for cross diffusion was used in the simulations.

#### 2.2.2 | Sensitivity Analysis

A sensitivity analysis was carried out with Ansys optiSLang software version 2024 R1 [29] coupled with TC-Prisma using the TC–Python interface [30]. Ten input parameters necessary for TC-Prisma setup were redefined as input variables in optiSLang and assigned a range of variation to generate combinations of these input variables, creating designs. TC-Prisma routines are called for each design (parallelization was used) to simulate the precipitation evolution and calculate the mean square error (MSE) of the volume fraction by comparing with the experimental phase volume fraction. A total of 10,000 designs were analyzed in optiSLang to evaluate the correlation between input variables and MSE responses of the phase volume fraction. A dynamic, space-filling Latin Hypercube Sampling approach [29] was used to sample the design variation space. The interoperative framework applied for the calculation workflow is shown in Figure 1.

Three time-regions were selected along the precipitation curve to analyze the effect of the input parameters: region 1, the initial stage where mostly nucleation occurs, region 2, where precipitate growth is significant, and region 3, the final stage toward the end of the annealing time. The MSE in these three time ranges to evaluate deviations from experiments caused by varying the input parameters.

## 3 | Results

### 3.1 | Microstructure Characterization

The LPBF Ti-21Al-25Nb (at.%) alloy in the as-built condition consists of a $\beta/\beta_o$ matrix with grains elongated in the vertical built direction across the melt pool boundaries (Figure 2a). The grain sizes are typically ∼20 μm perpendicular and 100–200 μm in the built direction. A nanoscale substructure with Nb-depleted areas indicating local segregation is recognized within the $\beta/\beta_o$ grains (Figure 2b). The segregated areas remain visible even after the annealing experiment for 180 min at 600°C, as shown in Figure 2c. The biphasic Widmanstätten microstructure after annealing reveals O-phase precipitates of lenticular shape and sizes up to ≃200–300 nm embedded in a $\beta/\beta_o$ matrix (Figure 2d).

### 3.2 | In Situ HEXRD

The HEXRD results show the single phase $\beta/\beta_o$-matrix in the as-built condition (Figure 3). The $\beta_o$−100 superlattice reflection, which is visible at the beginning of the in situ annealing experiment (inset of Figure 3a), suggests that ordering of the matrix phase (B2) occurred during LPBF. The degree of ordering is, however, not quantifiable from the experimental data.

The formation of O-phase can be recognized after ∼10 min when the $\beta_o$−100 superlattice reflection becomes weaker and disappears after ∼30 min. The evolution of the phase fraction of $\beta/\beta_o$ and O-phase, as well as the lattice parameter of the matrix, $a_\beta$, is depicted in Figure 3b. From the beginning of the annealing procedure until ∼25 min, the material shows a sluggish precipitation behavior consistent with previous investigations [18]. Thereafter, the O-phase volume fraction increases gradually until the end of the experiment, reaching 66 vol.% after 180 min. At this point, the HEXRD analysis evidences only two phases, namely β (A2) and O-phase. This is further discussed in Sections 4.1 and 4.2.

The lattice parameter of the matrix, $a_\beta$, increases during the whole experiment, with the strongest increase observed between

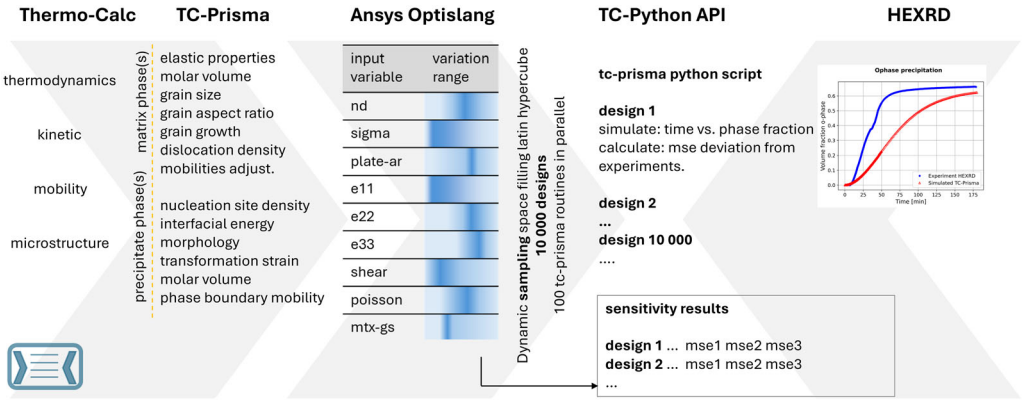



**FIGURE 1** | Calculation workflow for the sensitivity analysis showing the interoperability of the different codes combining simulations and experimental data.



15272648, 2026, 17, Downloaded from https://advanced.onlinelibrary.wiley.com/doi/10.1002/adem.70963 by Dtsch Zentrum F. Luft-U. Raum Fahrt In D. Helmholtz Gemein., Wiley Online Library on [06/10/2026]. See the Terms and Conditions (https://onlinelibrary.wiley.com/terms-and-conditions) on Wiley Online Library for rules of use; OA articles are governed by the applicable Creative Commons License

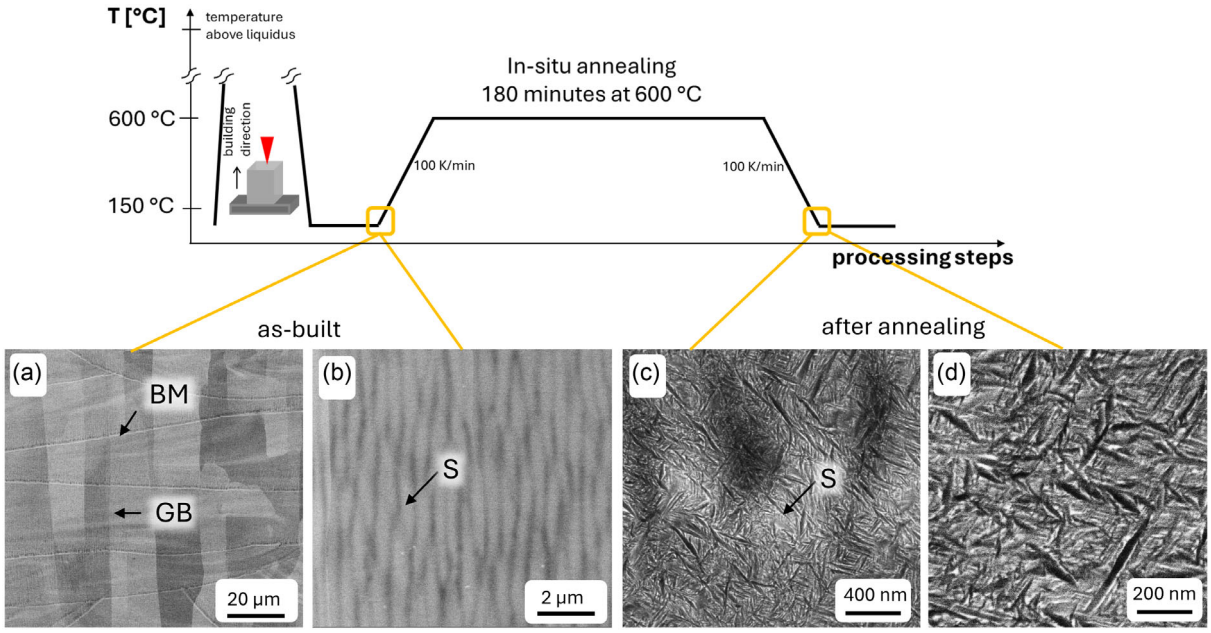



**FIGURE 2** | Process history and microstructure of the Ti-21Al-25Nb (at.%) alloy in LPBF as-built and after subsequent annealing during 180 min at 600°C. (a) As-built microstructure showing GB and bottoms of melt pools (BM). (b) Local segregation (S) within $\beta/\beta_o$ grain. (c) Widmanstätten microstructure after annealing with remaining segregation (S). (d) Precipitates of O-phase (dark) within $\beta$matrix (bright).

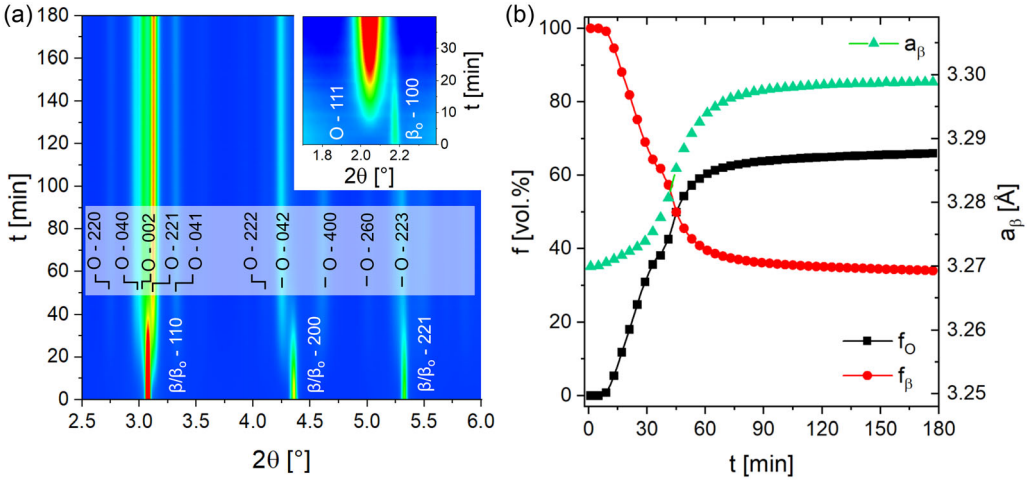



**FIGURE 3** | HEXRD synchrotron measurement of Ti-21Al-25Nb at.% processed with LPBF (Ev = 89 J/mm$^3$). (a) Evolution of HEXRD reflections during isothermal annealing at 600°C for 180 min. (b) Phase fractions of O-phase and $\beta/\beta_o$ as well as lattice parameter $a_\beta$ versus precipitation time determined from HEXRD.

~30 and 60 min. The variation of the lattice parameter during annealing is related to the composition changes during the $\beta/\beta_o$ to O-phase transformation taking place. The increase of $a_\beta$ can be explained by the redistribution of the smaller Al atoms from the supersaturated $\beta/\beta_o$ matrix to the O-Phase. The initial degree of Al supersaturation in the matrix was calculated from the overall composition, $\overline{C_{Al}}$, referred to the calculated equilibrium composition, $C_{eq,Al}$, of $\beta_o$ (B2) at 600°C (Table 1). In addition, relevant microstructural features from our previous study [11] are used to validate/compare with the simulation results and are summarized in Table 1.

### 3.3 | Stable and Metastable Thermodynamic Calculations

Thermodynamic calculations were carried out to get information on phase volume fractions, type of phase transformations, transformation temperatures, composition, and elemental distribution in the constituent phases. This information is relevant for a correct setup of the precipitation simulations. More fundamental information is also calculated from thermodynamics in each precipitation simulation run, i.e., the driving forces for nucleation and the driving forces for diffusion.



15272648, 2026, 17, Downloaded from https://advanced.onlinelibrary.wiley.com/doi/10.1002/adem.70963 by Dtsch Zentrum F. Luft-U. Raum Fahrt In D. Helmholtz Gemein., Wiley Online Library on [06/10/2026]. See the Terms and Conditions (https://onlinelibrary.wiley.com/terms-and-conditions) on Wiley Online Library for rules of use; OA articles are governed by the applicable Creative Commons License

Metastable calculations (by disregarding phases in the calculation script) were carried out to set conditions closer to the experiments. However, discrepancies between metastable equilibrium and experiments indicate the need to account for kinetics, as it will be shown in Section 3.4. In particular, the calculated O-phase fraction is far from the experimental value of 66 vol.% obtained after 180 min of annealing at 600°C.

The diagrams in Figure 4a show the volume fractions of the O-phase, β (A2), $\beta_o$ (B2), and liquid, as well as the site occupancies in the β and $\beta_o$ matrix calculated for the Ti-21Al-25Nb (at.%) alloy. The presence of a β (BCC_A2) phase below 500°C is a consequence of disregarding phases in metastable calculations. The two-phase transformations of interest are

$$\beta \leftrightarrow \beta_o \quad (1)$$

$$\beta_o \leftrightarrow O \quad (2)$$

Equation (1) is a second-order transformation (no phase coexistence) and Equation (2) is a first-order transformation (phase coexistence) for the Ti-21Al-25Nb at.% composition. From high to low temperatures, the $\beta \rightarrow \beta_o$ (A2 → B2) transition starts at 1165°C, indicating the need for chemical ordering before O-phase precipitation. Afterwards, the $\beta_o \rightarrow O$ transformation begins at a solvus temperature of 957.8°C. The phase fraction of the O-phase increases until reaching a maximum of 97% at 342.5°C. The computed O-phase fraction at 600°C is 83 vol.%, which is higher than the experimental value of 66 vol.%, pointing out the need for kinetic simulations.

The matrix disorders again as the $\beta_o \rightarrow \beta$ (B2 → A2) begins at 670°C, remaining disordered until room temperature, where two phases coexist, O-phase and β (A2). The experimental observations also show O-phase and β at room temperature after the annealing stage, and the disappearance of the $\beta_o$−100 superlattice reflection before the O-phase precipitation (Figure 3), probably indicating the beginning of the $\beta_o \rightarrow O$ transformation.

The chemical ordering of the $\beta_o$ (B2) parent phase is shown in Figure 4b, where the sub-lattice (SL) occupancies as a function of temperature can be seen for the three elements Al, Ti, and Nb. The thermodynamic model for $\beta_o$ (B2) has 2 SL (Figure 4b–d), if both SL have identical occupancy, the phase is completely disordered β (A2); if the occupancies differ, the phase is the ordered $\beta_o$ (B2). Ordering begins at 1165°C and increases gradually, reaching a maximum that coincides with the O-phase solvus temperature. Afterward, its ordering decreases again until a fully

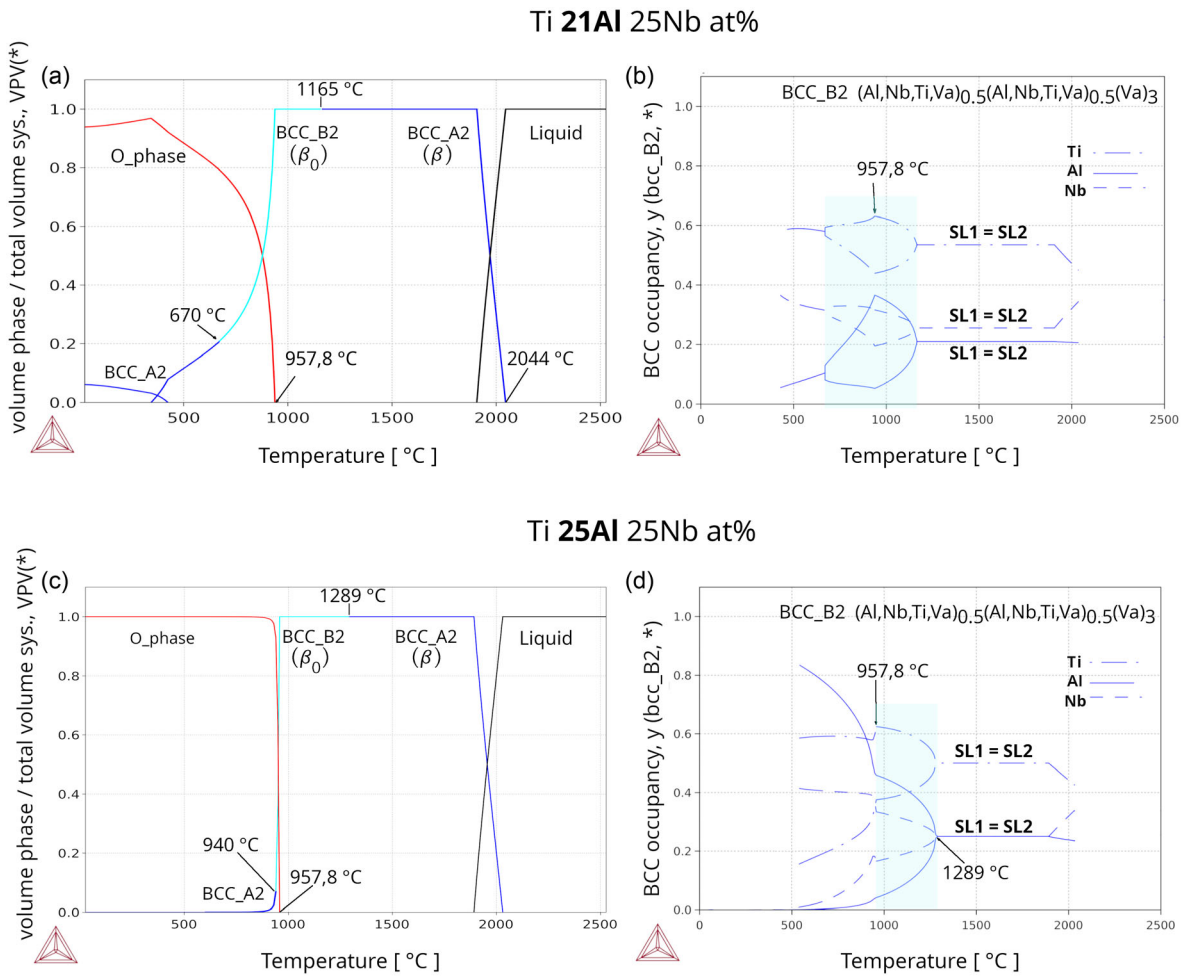



**FIGURE 4** | Calculated property diagrams for the Ti-21Al-25Nb (at.%) alloy, (a,b), and for the Ti-25Al-25Nb (at.%) alloy, (c,d), suspending all other phases except liquid, $\beta$(A2), $\beta_o$(B2), and O-phase, using TC version 2025a and TCTI6. One thermodynamic model is used to describe the B2 and A2 order/disorder in the BCC phase with 3 SL, inset of (b) and (d).



15272648, 2026, 17, Downloaded from https://advanced.onlinelibrary.wiley.com/doi/10.1002/adem.70963 by Dtsch Zentrum F. Luft-U. Raum Fahrt In D. Helmholtz Gemein., Wiley Online Library on [06/10/2026]. See the Terms and Conditions (https://onlinelibrary.wiley.com/terms-and-conditions) on Wiley Online Library for rules of use; OA articles are governed by the applicable Creative Commons License

disordered β (A2) phase is formed, which is thermodynamically stable from 670°C until room temperature. The light blue area determines the temperature range where the O-phase can transform from $\beta_o$ (B2) parent phase.

Corresponding metastable calculations for the Ti-25Al-25Nb at.% alloy were carried out to obtain a full picture. This composition corresponds to the ideal stoichiometry of the O-phase. The diagrams in Figure 4c,d show the $\beta \rightarrow \beta_o$ transformation starting at 1289°C, an O-phase solvus at 957.8°C, and a complete consumption of $\beta_o$ by the $\beta_o \rightarrow \beta$ transformation at 940°C. The phase field of coexistence, $\beta_o$ and O-phase, presents a very narrow temperature range for this alloy composition. The light blue areas of phase coexistence and the temperatures of the order-disorder transitions are relevant for the design of tailored microstructures.

**TABLE 2** | Input parameters for precipitation simulations and range of variation for sensitivity analysis.

| Input parameter | Selected values | Range for sensitivity analysis | Comment/references |
|---|---|---|---|
| (*1*) *MATRIX PHASE - BCC* | | | |
| grain size [μm] | 100 | 80–500 | |
| grain aspect ratio | 2.0 | 1.8–4.0 | |
| grain growth model | inactive | — | No grain growth during annealing. |
| dislocation density [$m^{-2}$] | 5.0E12 | 1E10–8E15 | Only varied for precipitation in dislocation settings, otherwise constant. |
| isotropic shear modulus [GPa] | 45 | 36–48 | |
| Poisson's ratio | 0.30 | 0.25–0.35 | |
| molar volume matrix [$m^3$/mol] | 1.079E-5 | constant | Calculated with TCTI6. |
| atomic mobility adjustment[a] | same for all three elements | — | Values from mobility database MOBTI5. |
| (*2*) *PRECIPITATE PHASE - O-PHASE* | | | |
| nucleation sites density [$m^{-3}$] | 4.5E18 | 3.8E17–3.0E25 | |
| IE prefactor | 1.23 | 1.10–1.43 | IE (TCTI6) $\sigma_{B2/O} = 0.048$ J/$m^2$. |
| growth rate model | general | — | Options are simplified, general, advanced[b]. |
| plate aspect ratio | 4.8 | 3.0–5.5 | Options are plate or needle[c]. |
| transformation strain, $\in_{11}$, | −0.064 | −0.0700–−0.05751 | Selected value determined from experiments in this work. |
| transformation strain, $\in_{22}$, | 0.031 | 0.0299–0.0400 | Selected value determined from experiments in this work. |
| transformation strain, $\in_{33}$ | 0.0056 | 0.00504–0.0119 | Selected value determined from experiments in this work. |
| molar volume precipitate [$m^3$/mol] | 9.178E-6 | constant | Calculated with TCTI6. |
| phase boundary mobility [$m^4$/Js] | 10 | constant | Default value. |
| phase energy addition [J/mol] | 0 | — | |
| approximate driving force | inactive | — | |
| preexisting size distribution | inactive | — | No preexisting precipitate distribution |
| (*3*) *PROCESSING PARAMETERS* | | | |
| isothermal precipitation, [K] | 873.15 | — | |
| simulation time, [min] | 180 | — | Isothermal annealing. |
| alloy constitution[d] | Ti-21Al-25Nb (at.%), A2, B2 and O-phase | | |

[a]No fast diffuser elements, same prefactor 1 for all elements.
[b]Convergence difficulties.
[c]Only options that allow the transformation strains as input parameters.
[d]Composition and phases.



15272648, 2026, 17, Downloaded from https://advanced.onlinelibrary.wiley.com/doi/10.1002/adem.70963 by Dtsch Zentrum F. Luft-U. Raum Fahrt In D. Helmholtz Gemein., Wiley Online Library on [06/10/2026]. See the Terms and Conditions (https://onlinelibrary.wiley.com/terms-and-conditions) on Wiley Online Library for rules of use; OA articles are governed by the applicable Creative Commons License

### 3.4 | Precipitation Simulations

Precipitation kinetics involves nucleation, growth, and coarsening stages, typically occurring as simultaneous processes in real materials, which makes individual onsets identification extremely difficult. The evolution of the O-phase fraction during the annealing experiment for 180 min. at 600°C was simulated from the supersaturated matrix $\beta/\beta_o$ (A2/B2) and compared with the HEXRD results (Table 1) to validate the simulations. To this purpose, the precipitation kinetics was considered as concomitant processes within TC-Prisma that couple thermodynamic and kinetic models.

The input parameters for precipitation simulations used in this work are presented in Table 2, divided into three groups: (1) processing, (2) matrix phase, and (3) precipitate phase. "Selected values" are those parameter values that allow the simulated precipitation evolution to better match the experimental results. A detailed discussion on the selection of these values is given in Section 4.2.

The precipitation evolution is computed using these values (Figure 5a, red line) and compared with the experiments (blue symbols). A 10% deviation from the experimental values is indicated with light gray symbols. The fairly good agreement shows that TC-Prisma kinetic models with realistic input parameters can reproduce the precipitation of the O-phase in the LPBF Ti-21Al-25Nb (at.%) alloy and provide information about the precipitate size, matrix composition, driving force, and supersaturation evolution.

The evolution of the precipitate size and distribution gives relevant information, for example, about the coarsening regime. Typically, when the critical radius of the precipitates reaches the average radius, the coarsening stage is reached. Larger particles grow at the expense of smaller ones, leading to a widening of the particle size distribution (PSD) and often to a decrease in the number of particles per volume (precipitate number density), and no further nucleation takes place. Usually, the coarsening process is considered toward the latest stages of the precipitation, but it can actually overlap with the growth stage or even the nucleation period [28].

However, the simulated evolution of the mean and critical precipitate radii (Figure 5b) increases with time, but the critical radius does not reach the mean radius value at 180 min.

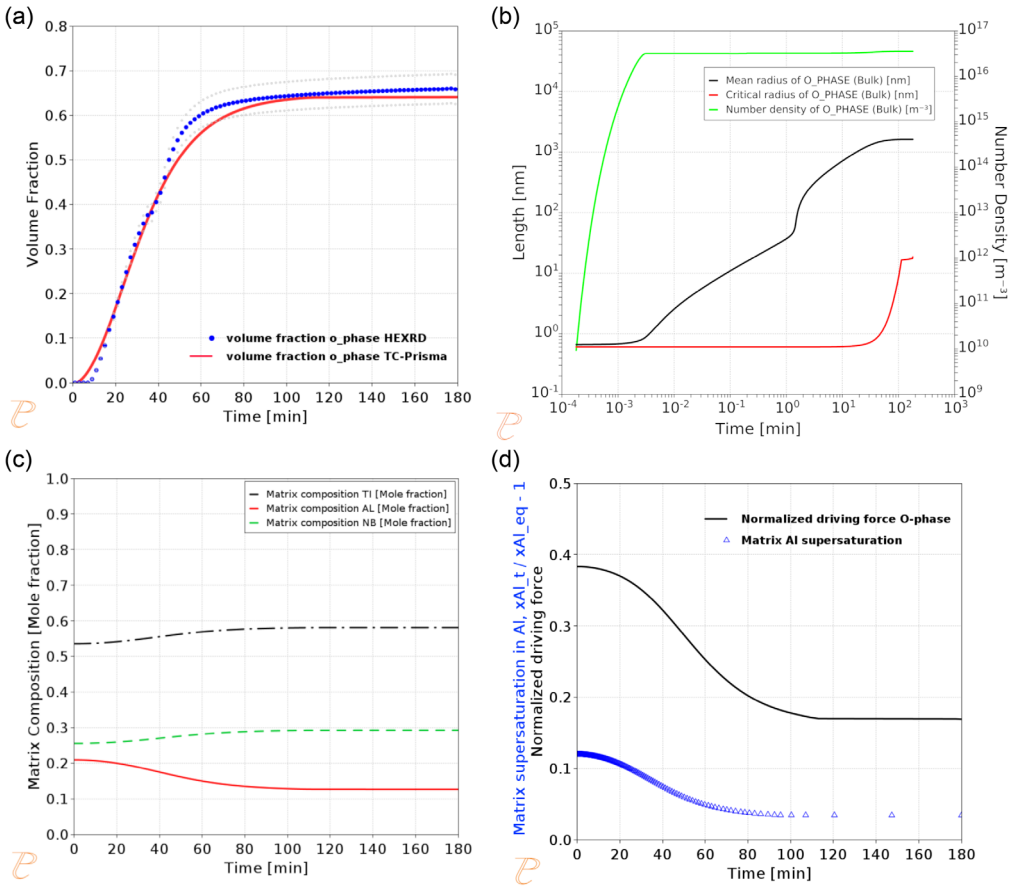



**FIGURE 5** | Results of the simulations for the isothermal precipitation simulation at 600°C of the O-phase from $\beta/\beta_o$(A2)/(B2) matrix in the Ti-21Al-25Nb (at.%) alloy. Simulations using TC-Prisma 2025a and TCTI6/MOBTI5. (a) O-phase volume fraction evolution (red line) superposed to experimental data from HEXRD (blue symbols) and 10% deviation from experimental curve (light gray symbols). (b) Evolution of the mean and critical radius of the O-phase plate-like precipitates. (c) Matrix composition evolution during precipitation of O-phase. (d) Correlation between the O-phase nucleation driving force and the matrix Al supersaturation evolution, $x_{Al,t}$mole fraction of Al during precipitation divided by $x_{Al,eq}$mole fraction Al in equilibrium for the $\beta$(A2) matrix at 600°C.



15272648, 2026, 17, Downloaded from https://advanced.onlinelibrary.wiley.com/doi/10.1002/adem.70963 by Dtsch Zentrum F. Luft-U. Raum Fahrt In D. Helmholtz Gemein., Wiley Online Library on [06/10/2026]. See the Terms and Conditions (https://onlinelibrary.wiley.com/terms-and-conditions) on Wiley Online Library for rules of use; OA articles are governed by the applicable Creative Commons License

Moreover, the number density increases, remaining practically constant during the aging, thus one can infer that the coarsening process has not yet started while nucleation is still taking place (Figure 5b). The mean radius for needle- and plate-like precipitates in this analysis is derived from a sphere with equivalent volume [31].

The simulated evolution of the matrix composition during O-phase precipitation is shown in Figure 5c. The strongest variation is found for Al, whose mole fraction decreases from 21 at.% to 12.4 at.%, although it does not reach the equilibrium value of 8.9 at.% calculated at 600°C (Figure S2). This change in Al composition during the precipitation of the O-phase correlates with the increase of the $\beta/\beta_o$ lattice parameter observed experimentally (Figure 3b). As Al is depleted from the matrix to form the O-phase, the β matrix becomes enriched in Ti (58 at.%) and Nb (29 at.%), while the Ti/Nb ratio remains nearly constant at ∼2. This enrichment explains the increase in lattice parameter observed experimentally (Figure S2).

Figure 5d shows the correlation between the instantaneous driving force for O-phase nucleation in the $\beta/\beta_o$ (A2/B2) matrix, normalized by RT (R the gas constant and T the temperature in K - dimensionless-), and the evolution of the degree of Al supersaturation in the matrix. The latter is given by the simulated evolution of the Al composition in mole fraction of Al, $x_{Al}$, divided by the calculated Al equilibrium composition in the matrix, $x_{eq,Al}$, at 600°C. The result clearly shows that the high matrix supersaturation in Al achieved by the LPBF process (i.e., due to nonequilibrium solidification) is the driving force for nucleation of the O-phase in the annealing stage.

### 3.5 | Sensitivity Analysis

To quantify the influence of each input parameter in the precipitation simulations, a sensitivity analysis was carried out over the O-phase fraction evolution using the calculation workflow described in Section 2.2 and in Figure 1. Ten input parameters were chosen: O-phase nucleation sites density, IE, O-phase plate aspect ratio, transformation strains ($\in_{11}$, $\in_{22}$, $\in_{33}$), matrix shear modulus, matrix Poisson's ratio, matrix grain size, and aspect ratio. The variation ranges are indicated in Table 2.

The result from the sensitivity analysis is presented in Figure 6: (a) as a summary of the effects in the three regions is indicated, and (b) as a correlation matrix that quantifies the relation of the responses to the input variables in the three regions as MSE1, MSE2, and MSE3. The sign of the correlation can be disregarded only accounting for the absolute values, for example, the nucleation density effect is highest on MSE1. Green indicates a low and blue a high correlation, respectively.

Figure 6a,b indicates that the initial stage of the precipitation (region 1) is mostly affected by the ND and the IE; both parameters are related to the nucleation conditions. Region 2 is mostly by the IE, the strain coefficient, $\in_{11}$, of the transformation matrix, the shear modulus, and the morphology of the precipitate (plate, needle, sphere). These parameters are related to the growth process and the precipitate's shape. Finally, region 3 of the precipitation evolution is strongly affected by the IE followed by the $\in_{11}$ strain coefficient and shear modulus. The latter is related to the elastic properties of the matrix and precipitate.

Other parameters shown in Figure 6a, although not defined as variables, are the processing temperature, the alloy composition, and the molar volume of the phases. The molar volumes were calculated from the experiments. The effect of changes in alloy composition or annealing temperature is high in region 3 because the main consequence is on the equilibrium phase fractions.

This sensitivity analysis framework can be extended to other kinetic outputs from simulations, such as PSD, critical radius, number density, and matrix composition, where the effect of the input settings seems less intuitive.

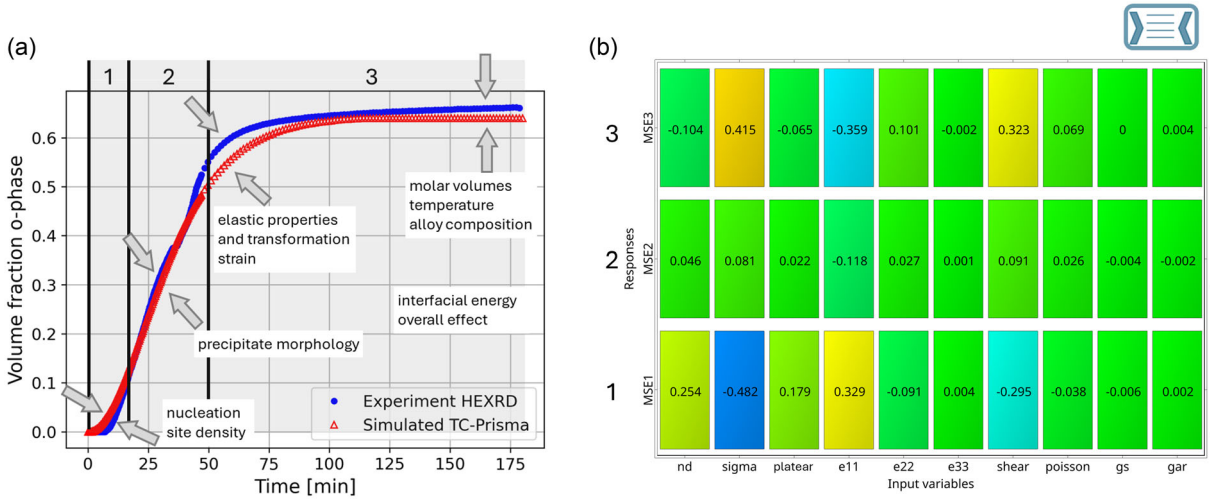



**FIGURE 6** | Results from the sensitivity analysis, (a) summary of the effect of input parameters on the three sections of the O-phase precipitation curve in Ti-21Al-25Nb (at.%) and (b) linear correlation matrix output from the calculation framework in Figure 1 showing correlation of the MSE response in the three regions of interest with the input variables: nucleation density (nd), IE prefactor (sigma), precipitate plate-like aspect ratio (platear), transformation strain coefficients (e11, e22, e33), shear modulus (shear), Poisson ratio (poisson), matrix grain size (gs) and matrix grain aspect ratio (gar).



15272648, 2026, 17, Downloaded from https://advanced.onlinelibrary.wiley.com/doi/10.1002/adem.70963 by Dtsch Zentrum F. Luft-U. Raum Fahrt In D. Helmholtz Gemein., Wiley Online Library on [06/10/2026]. See the Terms and Conditions (https://onlinelibrary.wiley.com/terms-and-conditions) on Wiley Online Library for rules of use; OA articles are governed by the applicable Creative Commons License

## 4 | Discussion

### 4.1 | Thermodynamics of the $\beta_o \rightarrow$ O Phase Transformation

Under the LPBF processing condition studied in this work, the $\beta_o \rightarrow$O transformation in the Ti-21Al-25Nb alloy observed experimentally is consistent with the thermodynamic calculations, indicating coexistence of β (A2) and O-phase after 180 min at 600°C. Experimentally, no $\beta_o$ (B2) reflections were observed after aging, providing strong evidence that the $\beta_o \rightarrow O$ and/or $\beta_o \rightarrow \beta$ phase transformations took place during precipitation. Our results further indicate that the transformation $\beta_o \rightarrow O$ is accompanied by compositional changes in the matrix, as reflected by the increase in the β lattice parameter $a_\beta$ observed experimentally.

The fact that the $\beta_o$−100 superlattice reflection was observed by HEXRD in the LPBF as-built condition may be related to the presence of $\beta_o$ (B2) stable at higher temperatures and retained at room temperature owing to the high cooling rates of the LPBF process (≈$10^6$ K/s). As shown in the inset of Figure 3a, the $\beta_o$ reflection disappears at the onset of O-phase precipitation, which is in agreement with previous investigations that postulate a need for ordering for the transformation to occur [18, 20, 32].

In line with the approach of transformation paths by Bendersky et al. [18], which can be analyzed by crystallographic relations of space groups, possible transformation paths for this case study is presented in Figure 7, where the crystal structures sequence of β (A2), $\beta_o$ (B2), and O-phase are shown. In B2, Al and Nb are mixed in *1b* position and have to redistribute during the phase transformation in the O-phase as Al in *4c1* and Nb in *4c2*.

### 4.2 | Precipitation Simulations

#### 4.2.1 | Criteria for Selection of Input Parameters

**4.2.1.1 | Nucleation Sites and Nucleation Density.** Although previous experiments at different conditions show O-phase precipitation at low-angle grain boundaries (LAGB) [11], bulk sites for precipitation were assumed in order to take into account different precipitate morphologies and the transformation strains. This is only possible for bulk nucleation due to limitations of the modified Langer–Schwartz theory and the Kampmann–Wagner method. The actual transformation strains were calculated from the experimental lattice parameter measurements (see Table 2).

Different nucleation-site types correspond to different energetic conditions and different numbers of available sites per volume, i.e., different ND, which directly influence the nucleation rate. As ND, fewer sites are available and, as a consequence, the precipitation curve shifts, delaying the nucleation stage.

To ensure realistic nucleation site densities, precipitation in dislocations was assumed to estimate the ND upper and lower bounds from the matrix dislocation density. The matrix dislocation density was varied in a range between $1 \times 10^{10}$ and

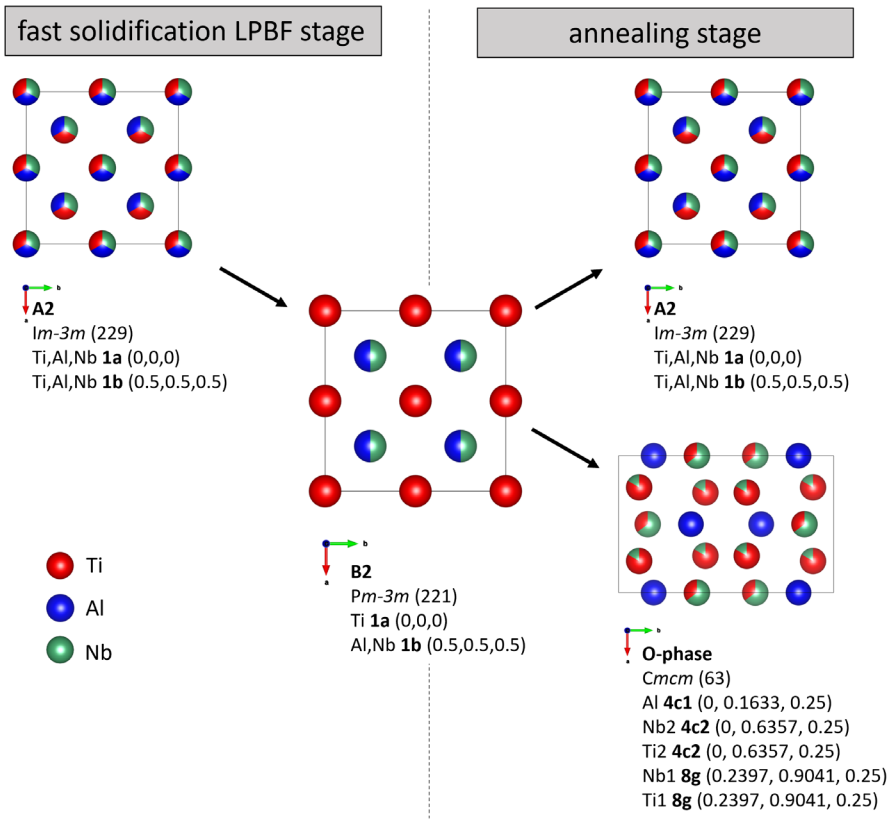



**FIGURE 7** | Possible transformation paths for the LPBF and postprocessing of the Ti-21Al-25Nb (at.%) alloy in line with the analysis of transformation paths by Bendersky et al. [18].



15272648, 2026, 17, Downloaded from https://advanced.onlinelibrary.wiley.com/doi/10.1002/adem.70963 by Dtsch Zentrum F. Luft-U. Raum Fahrt In D. Helmholtz Gemein., Wiley Online Library on [06/10/2026]. See the Terms and Conditions (https://onlinelibrary.wiley.com/terms-and-conditions) on Wiley Online Library for rules of use; OA articles are governed by the applicable Creative Commons License

$8 \times 10^{15} m^{-2}$[7, 33], which corresponds to an ND range between $3.8 \times 10^{19}$ and $3.0 \times 10^{25} m^{-3}$, respectively. The selected value that acceptably reproduces the beginning of the experimental precipitation curve is $4.5 \times 10^{18} m^{-3}$, which is within this range.

**4.2.1.2 | Interfacial Energy.** The IE is one of the most important input parameters because it has a strong effect on all the stages of precipitation. In the nucleation stage, it influences the Gibbs energy of formation of a critical nucleus, and thus the nucleation rate. In the growth stage, it relates to the different precipitate morphologies due to the interplay between the interfacial and elastic energy of matrix and precipitates, and in the coarsening stage, it is related to the rate constant (classical coarsening theory of Lifshitz–Slyozov–Wagner (LSW)). The IE characterizes the matrix/precipitates interface together with other properties like elastic constants (of matrix and precipitate), the misfit between β matrix and different O-phase crystallographic variants, and IE anisotropy. All these parameters play a role in shaping the precipitates and the resulting interfaces.

The sensitivity of the precipitation evolution to the IE was also confirmed by the sensitivity analysis, which underlines the need for realistic IE values. However, these are in many cases unavailable or only known for a few binary systems with fcc interfaces $\gamma/\gamma'$ (see e.g., Table 3).

The IE is a property that can not be measured directly being normally derived indirectly from experiments, e.g., from early nucleation or coarsening regimes [38]. Moreover, IE depends on several factors at the interface position, such as temperature, composition, entropy, interface coherency, atomic orientation, interface curvature, and interface width, among others.

The IE can be set as an input parameter in the precipitation simulations using TC-Prisma in the form of a prefactor or a function of the mean precipitate radius. The physical model implemented in TC is based on Becker's bond energy approach [39] modified by Turnbull [40] as shown in Equation (3).

$$\sigma_c = \frac{n_s \cdot z_s}{N_A \cdot z_l} \Delta E_s \tag{3}$$

where, $\sigma_c$ is the coherent IE between matrix and precipitate, $n_s$ is the number of atoms per unit of interface area, $z_s$ is the number of cross bonds per atom at the interface, $N_A$ is the Avogadro number, $z_l$ is the coordination number of an atom in the bulk crystal lattice, and $\Delta E_s$ is the energy of solution, which is calculated internally in TC-Prisma. This model assumes coherent interfaces, which is reasonable for the early stages of precipitation, but in many cases does not apply to later stages where the loss of coherency between matrix and precipitate can occur. In addition, this model has been developed for BCC and FCC structures for the (110)| (111) lattice planes, and all non-BCC phases are considered FCC for the calculation (O-phase in this case). The variation of the IE with the mean radius can be accounted for as a function; however in the present case, a closer fit to the O-phase volume fraction is obtained with a prefactor 1.23 corresponding to an IE value of $0.059\ J/m^2$.

The calculated IE for $\beta_o$ (B2)/O-phase is $0.042\ J/m^2$ at 600°C with Equation (3), which only depends on thermodynamic and atomic arrangements. This value, modified by the selected prefactor to account for kinetic effects on the IE, results in $0.059\ J/m^2$. The latter value accounts for several phenomena at the interface during a real precipitation process, changes in composition at the interfaces, atomic reorganization, effect of dislocations, loss of coherency, IE anisotropy, among others. An IE of $0.059\ J/m^2$ is relatively low, which can be expected from the orientation relation and possible coherency of these interfaces, see **Section Literature review** references [12, 18, 23] and Gussone et al. [11] Figure 8, where a TEM selected-area electron diffraction is shown related to the orientation relationship observed between O-phase and β matrix. Small lattice misfits, for example, lead to low interfacial energies below $0.1\ J/m^2$[28]. Values of IE for other systems are shown in Table 3.

As previously mentioned, the morphology of the precipitate is a result of the interplay between IE and the elastic energy. IE is

**TABLE 3** | Interfacial energies values for several material systems, calculated and experimentally determined.

| System | Interface | IE, $J/m^2$ | Temp., K | Comment/references |
|---|---|---|---|---|
| $Ti_2AlNb$/O-phase | BCC (110)/FCC (111) | 0.042 | 600 | Calculated TC this work Section 4.2.1. |
| $Ti_2AlNb$/O-phase | B2 (110)/O (001) | 0.58, 0.46, 0.41, 0.59[a] | 0 | Calculated DFT[b] [34] |
| $\gamma$-TiAl/$\gamma$-TiAl | $L1_0/L1_0$60°, 120°, 180° | 0.27, 0.25, 0.06 | 0 | Calculated DFT [35] |
| $\gamma$-TiAl/$\gamma$-TiAl | $L1_0/L1_0$(111) plane, 180° | 0.55, 0.06, 0.55[c] | 0 | Calculated DFT [35] |
| $\alpha_2$-$Ti_3Al$/$\gamma$-TiAl | $DO_{19}/L1_0$ | 0.126 | 0 | Calculated DFT [36] |
| Ni-Al | $\gamma$(A1)/$\gamma'$ ($L1_2$) | 0.02233, 0.01952 | 898, 988 | Experimental [37] |
| Ni-Ga | $\gamma$(A1)/$\gamma'$ ($L1_2$) | 0.0167 | — | Determined from experiments LSW [37] |
| Ni–Ti | $\gamma$(A1)/$\gamma'$ ($L1_2$) | 0.08397 | — | Determined from experiments LSW [37] |
| Ni-Si | Ni(Si) (A1)/$Ni_3Si$ ($L1_2$) | 0.06961 | 923 | Determined from experiments LSW [37] |
| Ni-Cu-Al | $\gamma$(A1)/$\gamma'$-$(Cu,Ni)_3Al$ ($L1_2$) | 0.052 | 823 | [28] |
| Fe-Cu | Fe-1.4Cu | 0.250 | 673 | [28] |

[a]Different stacking sites.
[b]Density Functional Theory (DFT).
[c]Fault energies, antiphase boundary APB, superlattice intrinsic stacking fault SISF and complex stacking fault CSF, respectively.



15272648, 2026, 17, Downloaded from https://advanced.onlinelibrary.wiley.com/doi/10.1002/adem.70963 by Dtsch Zentrum F. Luft-U. Raum Fahrt In D. Helmholtz Gemein., Wiley Online Library on [06/10/2026]. See the Terms and Conditions (https://onlinelibrary.wiley.com/terms-and-conditions) on Wiley Online Library for rules of use; OA articles are governed by the applicable Creative Commons License

minimized for spherical or faceted particles, while the elastic energy, which is related to the particle volume, is minimized for plate-like shapes. During the nucleation stage, the large interface to volume ratio leads to spherical precipitate shapes coherent with the matrix, but as the particles become larger in the growth and coarsening stages, there is normally a partial or total loss of coherency (semi-/incoherent) between matrix and precipitates. Thus, the IE anisotropy increases the overall IE with the particle size for plate and needle morphologies, defined by an aspect ratio length over diameter. Wu et al. [31] clearly show that the IE increases with the aspect ratio of the particles, whereas the elastic strain energy decreases. With the simulation settings used in this work, i.e., IE and aspect ratio independent of the mean particle size, the previously mentioned effects were not taken into account, leading to an overestimation of the mean particle size and underestimation of the aspect ratio toward the end of the annealing process.

**4.2.1.3 | Elastic Properties of the Matrix and Precipitates.** During the nucleation stage, the energetic barrier is dominated by the IE contribution. Since the initially formed precipitate clusters are normally coherent with the matrix, they are able to accommodate the strain resulting from the lattice misfit as elastic strain energy, minimizing this factor. However, as precipitates grow, the elastic strain energy becomes dominant. This is also observed in the simulations, where a variation of the matrix elastic properties, i.e., the shear and Poisson modules, shifts the precipitation curve to lower O-phase volume fractions toward the end of the aging (Figure 6a). With a shear module of 45 GPa and a Poisson ratio of 0.3 [41], the elastic properties of the matrix β cubic phase, the simulations can reproduce the experimental curve with ∼66 vol.% fraction of O-phase at the end of the annealing heat treatment. The computed mean radius of 1000 nm seems slightly overestimated with respect to the experimentally observed radius of ∼500 nm (Figure 2) at the end of the aging because the IE and aspect ratio were considered independent of the mean particle size.

### 4.2.2 | Aspects of the Precipitation Curve

As already stated, the precipitation behavior of the O-phase can be described as sluggish when comparing simulation settings that lead to an almost instant equilibrium phase fraction. From the measured Al initial supersaturation in the matrix (Table 1), one can expect large driving forces for precipitation. This would imply fast precipitation kinetics of the O-phase with severe changes in composition, abundant nucleation sites, and rapid increase of the volume fraction toward the equilibrium fraction of ∼83 vol.% O-phase.

However, the O-phase fraction exhibits an initial delay of about 10 min (Figure 3). It then increases gradually up to ∼60 min, followed by a much slower increase, reaching 66 vol.% after 180 min of aging. Simulations with longer aging times were carried out to confirm the increase of phase fraction toward equilibrium (see Figure S1). The simulations show that the phase fraction tends to the equilibrium after ∼10,000 days. A possible explanation for this behavior is that the system experiences a saturation of nucleation sites at around 180 min: the mean radius is close to the critical radius, i.e., corresponding to a narrow PSD, leading to a very small growth rate. Gradually, the PSD widens up, and the particles can grow faster, reaching the coarsening stage close to the equilibrium value (Figure S1).

Another reason that may cause deviation of the phase fraction from the equilibrium value after 180 min of aging is factors such as strains in the matrix (Table 1), as recently communicated in similar alloys [42], as well as interfacial effects, dislocations, LAGB defects, which have been reported to play a significant role in the nucleation of the O-phase [11, 43]. Interestingly, our analysis of sensitivity shows that the elastic properties of the matrix play an important role in the phase fraction value toward the latest stage of the precipitation.

Finally, in agreement with the aspects mentioned above, no coarsening stage seems to be taking place around 180 min into the annealing experiment. The lack of coarsening can also be inferred from the simulation results, Figure 5b, because the critical radius does not reach the value of the mean radius of the O-phase precipitates.

## 5 | Conclusions

We present a calculation framework that enabled us to explain the precipitation behavior of the O-phase during postprocessing of LPBF-manufactured Ti-21Al-25Nb (at.%) alloy. This framework builds on the close combination of experimental studies with simulation methods based on thermodynamic models. Confidence in the significance of the results obtained from the thermodynamic computations was gained with a thorough sensitivity analysis of the input parameters used in the simulation. The simulation results were validated by a comparison with the experimental data obtained by in situ high-energy X-ray diffraction.

The simulations of the precipitation behavior in conjunction with experimental studies allowed us to understand:

1. Several aspects of the O-phase precipitation evolution, such as initial delay, sluggish behavior along the whole aging time, no coarsening after 180 min of annealing at 600°C, and composition changes during precipitation.
2. That the high Al supersaturation of the matrix obtained after the additive manufacturing is the driving force for the subsequent isothermal precipitation of the O-phase.
3. That the $\beta \leftrightarrow \beta_o$ transformation plays a significant role in the precipitation of the O-phase that can be used to engineer microstructures in $Ti_2AlNb$ alloys.
4. The sensitivity analysis provides insights into the influence of the input parameters driving the precipitation behavior.
5. The assessment of the input parameters indicates that the IE between the matrix and the precipitates is the most relevant parameter, having a strong influence on the whole precipitation sequence.

Providing the proper input parameters in the simulations' setup is hence a prerequisite to ensure that the computational



15272648, 2026, 17, Downloaded from https://advanced.onlinelibrary.wiley.com/doi/10.1002/adem.70963 by Dtsch Zentrum F. Luft-U. Raum Fahrt In D. Helmholtz Gemein., Wiley Online Library on [06/10/2026]. See the Terms and Conditions (https://onlinelibrary.wiley.com/terms-and-conditions) on Wiley Online Library for rules of use; OA articles are governed by the applicable Creative Commons License

results and extrapolation to predictive conditions lead to meaningful results.


### Acknowledgments

The authors acknowledge Andre Schneider and Nicholas Grundy from TC Software AB. S.T. and S.G.F. acknowledge Prof. Qing Chen from K.T.H. for the useful discussions. S.G.F. acknowledges the use of the facilities of ZGH (Center for Interface-Dominated High-Performance Materials in Ruhr University Bochum). DESY is acknowledged for the provision of synchrotron facilities at PETRAIII beamline P07 in the frame of proposal I-20191042.

Open Access funding enabled and organized by Projekt DEAL.

### Funding

This work was supported by Deutsches Elektronen-Synchrotron (Grant I-20191042).


### Conflicts of Interest

The authors declare no conflicts of interest.

### Data Availability Statement

The data that support the findings of this study are available from the corresponding author upon reasonable request.

### References


1. Z. Liang, I. Zhirnov, F. Zhang, et al., "Development of Computational Framework for Titanium Alloy Phase Transformation Prediction in Laser Powder-Bed Fusion Additive Manufacturing," *Materialia* 14 (2020): 100934.

2. R. Hu, K. Zhang, H. Zou, et al., "Research Progress on $Ti_2AlNb$-Based Alloys and Composites for Aerospace Applications," *Journal of Alloys and Compounds* 1021 (2025): 179701.

3. Y. Zhu, F. Wang, S. Jia, et al., "Process-Structure Relationship and Microstructure Evolution of Ti–22Al–25Nb Alloy Under Heat Treatment,"*Materials Chemistry and Physics* 343 (2025): 131006.

4. J. O. Andersson, T. Helander, L. Höglund, P. Shi, and B. Sundman, "Thermo-Calc and DICTRA, Computational Tools for Materials Science," *Calphad: Computer Coupling of Phase Diagrams and Thermochemistry* 26, no. 2 (2002): 273, iSBN: 03645916.

5. Thermo-Calc Software AB, Precipitation Module (TC-PRISMA) User Guide 2025a, URL https://thermocalc.com/wp-content/uploads/Documentation/Current_Static/precipitation-module-tc-prisma-user-guide.pdf.

6. E. Kozeschnik, J. Svoboda, P. Fratzl, and F. D. Fischer, "Modelling of Kinetics in Multi-Component Multi-Phase Systems With Spherical Precipitates: II: Numerical Solution and Application," *Materials Science and Engineering A* 385, no. 1-2 (2004): 157.

7. Y. Zhou, W. Li, D. Wang, et al., "Selective Laser Melting Enabled Additive Manufacturing of Ti–22Al–25Nb Intermetallic: Excellent Combination of Strength and Ductility, and Unique Microstructural Features Associated," *Acta Materialia* 173 (2019): 117.

8. Y. Zhou, W. Li, L. Zhang, et al., "Selective Laser Melting of Ti–22Al–25Nb Intermetallic: Significant Effects of Hatch Distance on Microstructural Features and Mechanical Properties," *Journal of Materials Processing Technology* 276 (2020): 116398.

9. A. G. Illarionov, S. I. Stepanov, I. A. Naschetnikova, et al., "A Review—Additive Manufacturing of Intermetallic Alloys Based on Orthorhombic Titanium Aluminide $Ti_2AlNb$," *Materials* 16, no. 3 (2023): 991.

10. J. Liao, A. Fan, H. Luo, and Y. Du, "Research Progress of Laser Powder Bed Fusion of $Ti_2AlNb$-Based Alloys: Microstructure, Defects, and Properties," *Journal of Materials Research and Technology* 35 (2025): 3393.

11. J. Gussone, M. W. Rackel, S. Tumminello, et al., "Microstructure Formation during Laser Powder Bed Fusion of Ti-22Al-25Nb with Low and High Pre-Heating Temperatures," *Materials & Design* 232 (2023): 112154.

12. D. Banerjee, A. K. Gogia, T. K. Nandi, and V. A. Joshi, "A New Ordered Orthorhombic Phase in a $Ti_3Al$ Nb Alloy," *Acta Metallurgica* 36, no. 4 (1988): 871.

13. B. Mozer, L. A. Bendersky, and W. J. Boettinger, "Neutron Powder Diffraction Study of the Orthorhombic $Ti_2AlNb$ Phase," *Scripta Metallurgica et Materiala* 24 (1990): 2363.

14. C. Boehlert, "The Phase Evolution, Creep and Tensile Behavior of Two-Phase Orthorhombic Titanium Alloys," (Doctor diss., University of Dayton, 1997).

15. C. J. Boehlert, B. S. Majumdar, V. Seetharaman, and D. B. Miracle, "Part I: The Microstructural Evolution in Ti-Al-Nb O + BCC Orthorhombic Alloys," *Matallurgical and Materials Transactions A* 30A (1999): 2305.

16. J. Kumpfert, "Intermetallic Alloys Based on Orthorhombic Titanium Aluminide," *Advanced Engineering Materials* 3 (2001): 11–851.

17. L. A. Bendersky, A. Roytburd, and W. J. Boettinger, "Transformation of BCC and B2 High Temperature Phases to HCP and Orthorhombic Structures in the Ti–Al–Nb System. Part I: Microstructural Predictions Based on a Subgroup Relation Between Phases," *Journal of Research of the National Institute of Standards and Technology* 98, no. 5 (1993): 561.

18. L. Benderskyand W. Boettinger, "Transformation of BCC and B2 High Temperature Phases to HCP and Orthorhombic Structures in the Ti–Al–Nb System. Part II: Experimental TEM Study of Microstructures," *Journal of Research of the National Institute of Standards and Technology* 98, no. 5 (1993): 585.

19. L. Bendersky, A. Roytburd, and W. Boettinger, "Phase Transformations in the $(Ti, Al)_3Nb$ Section of the Ti-Al-Nb System - I. Microstructural Predictions Based on a Subgroup Relation Between Phases," *Acta Metallurgica et Materialia* 42, no. 7 (1994): 2323.

20. L. A. Benderskyand W. J. Boettinger, "Phase Transformations in the $(Ti, Nb)_3Al$ Section of the Ti-Al-Nb System - II. Experimental TEM Study of Microstructures," *Acta Metallurgica et Materialia* 42, no. 7 (1994): 2337.

21. L. D. Landauand E. M. Lifshitz, *Statistical Physics*, 2ed. (Pergamon Press, 1969), 484.

22. J. H. Perepezko, *Intermetallic compounds, volume 1 - Principles*(John Wiley & Sons, Inc, 1995), 849–870, ISBN 0-471-94219-7.

23. F. A. Sadiand C. Servant, "On the B2→O Phase Transformation in Ti–Al–Nb Alloys," *Materials Science & Engineering A* 346 (2003): 19.

24. Thermo-Calc Software AB, Titanium and TiAl-based Alloys Databases (TCTI6), URL https://thermocalc.com/products/databases/titanium-and-titanium-aluminide-based-alloys/.

25. Thermo-Calc Software AB, Ti-alloys Mobility Database (MOBTI5), URL https://thermocalc.com/wp-content/uploads/Documentation/Databases/Mobility/mobti6-technical-info.pdf.

26. H. Lukas, S. G. Fries, and B. Sundman, *Computational Thermodynamics. The Calphad Method*(Cambridge University Press, 2007).

27. J. S. Langerand A. J. Schwartz, "Kinetics of Nucleation in Near-Critical Fluids," *Physical Review A* 21, no. 3(1980): 948.

28. R. Wagner, R. Kampmann, and P. W. Voorhees, *Phase Transformations in Materials*(Wiley-VCH Verlag GmbH, 2001), 713, prof. gernot kostorz edition, ISBN 3-527-30256-5.

29. Ansys OptiSLang 2024 R1, Dynardo GmbH, URL https://www.ansys.com/products/connect/ansys-optislang.





15272648, 2026, 17, Downloaded from https://advanced.onlinelibrary.wiley.com/doi/10.1002/adem.70963 by Dtsch Zentrum F. Luft-U. Raum Fahrt In D. Helmholtz Gemein, Wiley Online Library on [06/10/2026]. See the Terms and Conditions (https://onlinelibrary.wiley.com/terms-and-conditions) on Wiley Online Library for rules of use; OA articles are governed by the applicable Creative Commons License

30. Thermo-Calc Software AB, TC-Python API 2025a, URL https://thermocalc.com/products/software-development-kits/tc-python/.

31. K. Wu, Q. Chen, and P. Mason, "Simulation of Precipitation Kinetics with Non-Spherical Particles," *Journal of Phase Equilibria and Diffusion* 39, no. 5 (2018): 571.

32. C. Servantand I. Ansara, "Thermodynamic Modelling of the Order–Disorder Transformation of the Orthorhombic Phase of the Al–Nb–Ti System," *Calphad: Computer Coupling of Phase Diagrams and Thermochemistry* 25, no. 4 (2001): 509.

33. Q. Zhang, H. Shen, Y. Yang, et al., "In-Situ TEM Study on the Effect of Dislocations on Phase Transformation and Cycling Behaviors of Laser Powder Bed Fused TiNi Alloy," *Journal of Alloys and Compounds* 1013 (2025): 178450.

34. A. Wang, P. Liu, J. Xie, D. Ma, and Z. Mao, "First-Principles Investigation on the Atomic Structure, Stability and Electronic Property of O(001)/B2(110) Interface in $Ti_2AlNb$ Alloys," *Journal of Alloys and Compounds* 817 (2020): 152734.

35. C. L. Fuand M. H. Yoo, "Interfacial Energies in Two-Phase TiAI-Ti3Al Alloy," *Scripta Materialia* 37, no. 10 (2008): 1453.

36. M. Kanani, A. Hartmaier, and R. Janisch, "Interface Properties in Lamellar TiAl Microstructures from Density Functional Theory," *Intermetallics* 54 (2014): 154.

37. A. J. Ardell, "A1-L12 Interfacial Free Energies from Data on Coarsening in Five Binary Ni Alloys, Informed by Thermodynamic Phase Diagram Assessments," *Journal of Materials Science* 46, no. 14 (2011): 4832.

38. A. J. Ardell, "Trans-Interface-Diffusion-Controlled Coarsening of $\gamma'$ Particles in Ni–Al Alloys: Commentaries and Analyses of Recent Data," *Journal of Materials Science* 55, no. 29 (2020): 14588.

39. R. Becker, "Die Keimbildung Bei der Ausscheidung in Metallischen Mischkristallen," *Annalen der Physik* 424, no. 1-2 (1938): 128.

40. D. Turnbull, "Interfacial Energy," *Impurities and Imperfections* 638–642 (1955): 121.

41. A. Pathakand A. K. Singh, "A First Principles Study of $Ti_2AlNb$ Intermetallic," *Solid State Communications* 204 (2015): 9.

42. W. Tang, B. Shao, and Y. Zong, "The Effect of 0.02–0.37 Strain on the Precipitation Law of O Phase Colonies in $Ti_2AlNb$-Based Alloy during Aging," *Journal of Materials Research and Technology* 22 (2023): 89.

43. J. Lin, X. Sui, S. Cheng, G. Wang, and Z. Li, "Precipitation Mechanism of Nano-Size O Phase in Single B2 Phase $Ti_2AlNb$ Alloy," *Chinese Journal of Aeronautics* 38, no. 7 (2025): 103596.

## Supporting Information

Additional supporting information can be found online in the Supporting Information section.



15272648, 2026, 17, Downloaded from https://advanced.onlinelibrary.wiley.com/doi/10.1002/adem.70963 by Dtsch Zentrum F. Luft-U. Raum Fahrt In D. Helmholtz Gemein., Wiley Online Library on [06/10/2026]. See the Terms and Conditions (https://onlinelibrary.wiley.com/terms-and-conditions) on Wiley Online Library for rules of use; OA articles are governed by the applicable Creative Commons License